Strain energy-based fatigue failure analyses of LB-PBF Inconel 718: Effect of build orientation

Arash P. Jirandehi [a], Behnam Hajshirmohammadi [a], Patricio Carrion [b,c], M.M. Khonsari [a,*], Nima Shamsaei [b,c], Shuai Shao [b,c]

[a] Department of Mechanical and Industrial Engineering, Louisiana State University, Baton Rouge, LA 70803, USA
[b] National Center for Additive Manufacturing Excellence, Auburn University, Auburn, AL 36849, USA
[c] Department of Mechanical Engineering, Auburn University, Auburn, AL 36849, USA

ARTICLE INFO

ABSTRACT

Additively manufactured Inconel 718 parts fabricated in three build orientations (horizontal, vertical, and angled at 45 degrees) are tested in fully-reversed bending fatigue mode. Damping measurements via the Impulse Excitation technique are used to assess the defects content in the microstructure and fractography analysis is performed to detect the root cause of failure. Two micro- and macro-scale methodologies of fatigue damage estimation based on the dissipated heat per cycle and the statistical estimation of micro-plastic strain energies are used to assess fatigue damage. It is shown that at a given stress level, the vertically built specimens endure the most fatigue damage before failure while the diagonally built ones sustain the least. The fatigue life is estimated for arbitrary load amplitudes via a microstructure-sensitive algorithm with acceptable accuracy as compared to the experiments.

1. Introduction

The development of advanced materials and manufacturing techniques has become crucial in responding to the stringent operating conditions of many engineering systems. Such a stimulant has given rise to the rapid production of additively manufactured (AM) components with customized designs that promise superior performance. However, notwithstanding the enormous progress toward this objective, structural integrity and fatigue damage of AM components remain as major concerns [1–4].

Several recent investigations have assessed the fatigue performance of specimens manufactured with different AM processes [3,5–9]. Examination of the results reveals that the presence of volumetric defects formed during manufacturing processes is often the most influential factor on the fatigue performance of AM metals in the machined surface conditions. Hence, many studies on the fatigue assessment of AM components focus on the shape, size, distribution, population, and the location of these defects (e,g., pores, keyholes, and lack-of-fusion defects) or the effect of their movement on the nearby microstructure. Larger sizes, irregular shapes (particularly those with stress-concentration), and greater proximity to the free surface tend to increase the probability of volumetric defects to become the sites of crack(s) initiation under cyclic loading [10]. Nonetheless, the accumulation of cyclic slip irreversibility in the Persistent Slip Bands (PSBs) can still be the potential site for crack initiation in AM metallic alloys [11].

Yadollahi et al. [12] developed a statistical fatigue life prediction model for the as-built AM specimens based on the statistical distribution of defects shape and size. They indicated that the subsurface defects size is the most influential factor for fatigue lives below 1 million cycles. Sheridan et al. [13] studied the processing-structure-property-performance (PSPP) relationship in the additively manufactured Inconel 718 (IN718) alloy and postulated that the fatigue life may be strongly affected by the size and location of porosities. Bao et al. [14] studied Ti-6Al-4 V specimens fabricated via the laser beam powder bed fusion process (LB-PBF) and developed an algorithm with machine learning in an attempt to predict its fatigue life. They concluded that defects' location, shape, and size determine the fatigue life in the high-cycle fatigue (HCF) regime. To understand the fatigue behavior of an additively manufacture Al alloy, Haridas et al. [15] studied the LB-PBF Al–Cu-Sc-Zr specimens, and used a three-parameter Weibull function to account for the defects size distribution. They performed fatigue bending experiments to verify the proposed model and concluded that defects such as solid-state inclusions and pores are the

Nomenclature

A_k	Internal variables		std	Standard deviation
K	Hardening coefficient (MPa)		V_k	Internal variables
k	Thermal conductivity coefficient		W_p	Plastic strain energy per cycle (MJ/m³.cycle)
n	Hardening exponent		Y	True yield limit of an element (strain)
q	Dissipated heat		ε_p	Plastic strain
N_f	Fatigue life (Cycles)		σ	Stress (MPa)
T	Temperature (K)		α	Coefficient of std
S	Entropy		υ	Poisson's ratio
s	Slip direction		μ	Mean of strain
t_f	Time to failure		$\underline{\sigma}$	Stress (MPa)
			$\dot{\gamma}$	Entropy generation rate (MJ/m³.cycle)

Table 1

Different measures of damping and their relations [46].

| Specific damping (Ψ)	$\dfrac{1}{2Q}$	$\dfrac{\eta}{2}$
Quality factor (Q)	$\dfrac{1}{\eta}$	$\dfrac{1}{2\Psi}$
Loss factor (η)	$\dfrac{1}{Q}$	2Ψ

primary sites of crack initiation.

Research shows that build orientation is one of the parameters that affect the level and orientation of defects in AM parts [3,16]. Yadollahi et al. [17] studied the effect of build orientation on the fatigue of AM 17–4 PH stainless steel and reported that the average area of voids on the normal plane to the loading direction in vertically-printed specimens is almost double the size of that in the horizontally-built specimens, and this leads to their inferior fatigue performance. In another study, Yadollahi et al. [18] indicated that horizontally-printed 17–4 PH stainless steel specimens have higher fatigue strength than the vertically-printed specimens when uniaxially loaded along the longitudinal axis of the specimens. They concluded that the lack-of-fusion defects were most detrimental to fatigue due to their irregular shape, leading to higher stress concentration (as compared to spherical pores for instance). Nonetheless, they observed that cracks also initiate from smaller voids when in shorter fatigue life regimes. Ziółkowski et al. [19] conducted X-ray computed tomography (XCT) and microscopy on LB-PBF 316 L specimens in orientations of 0° (horizontal), 45° (diagonal), and 90° (vertical). Although the XCT indicated that the porosity content (population) in the horizontally-printed specimens is more than the vertically-printed and the angled ones, the microscopy analysis showed more porosity in vertically-printed specimens than the horizontally-printed and the angled ones. In both methods, however, the diagonal specimens contained the least pores population. Ziolkowski et al. associated the inconsistency in the measured values of vertically- and horizontally- printed specimens with the two methods to the inability of the XCT to capture the pores with less than 70 μm. Qian et al. [20] also showed that the porosity content in AM Ti-6Al-4 V specimens with 45° build orientation is less than that seen in horizontally- and vertically-printed specimens processed with LB-PBF process. Balachandramurthi et al. [21] investigated the LB-PBF Inconel 718 specimens in different build orientations. They reported that the highest elastic modulus, yield stress, and ultimate strength were obtained in specimens printed in a 45° direction. The lowest value of these properties is in the vertically-printed specimens. Peronat et al. [22], however, reported measuring the highest porosity content in the diagonally-printed Ti-6Al-4 V specimens (produced via LB-PBF) while the horizontally-printed specimens contained more porosity than the vertically-printed ones. Nonetheless, in their study, the horizontally printed specimens showed the best and vertically-printed specimens the worst fatigue performance. The above discussion suggests that the fatigue resistance is not merely a function of the percent porosity. Their shapes, sizes and distributions also play a role.

Table 2

The process parameters use for fabricating LB-PBF IN 718 specimens.

Parameter	Value	Unit
Laser Power	285	W
Scan Speed	960	mm/s
Hatch spacing	0.11	mm
Stripe width	10	mm
Layer thickness	0.040	mm
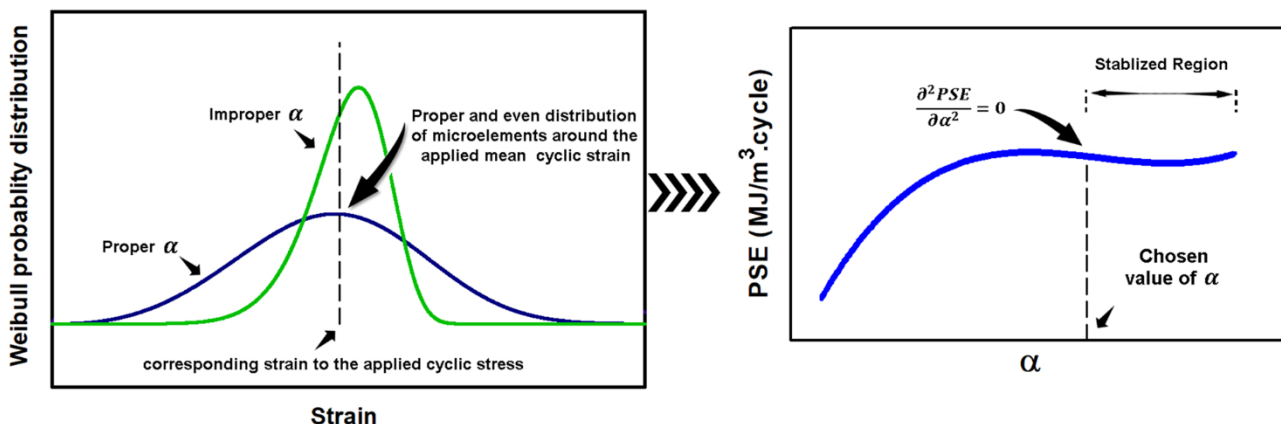
Fig. 1. The pictorial representation of the two standards for finding the correct choice of α [37].
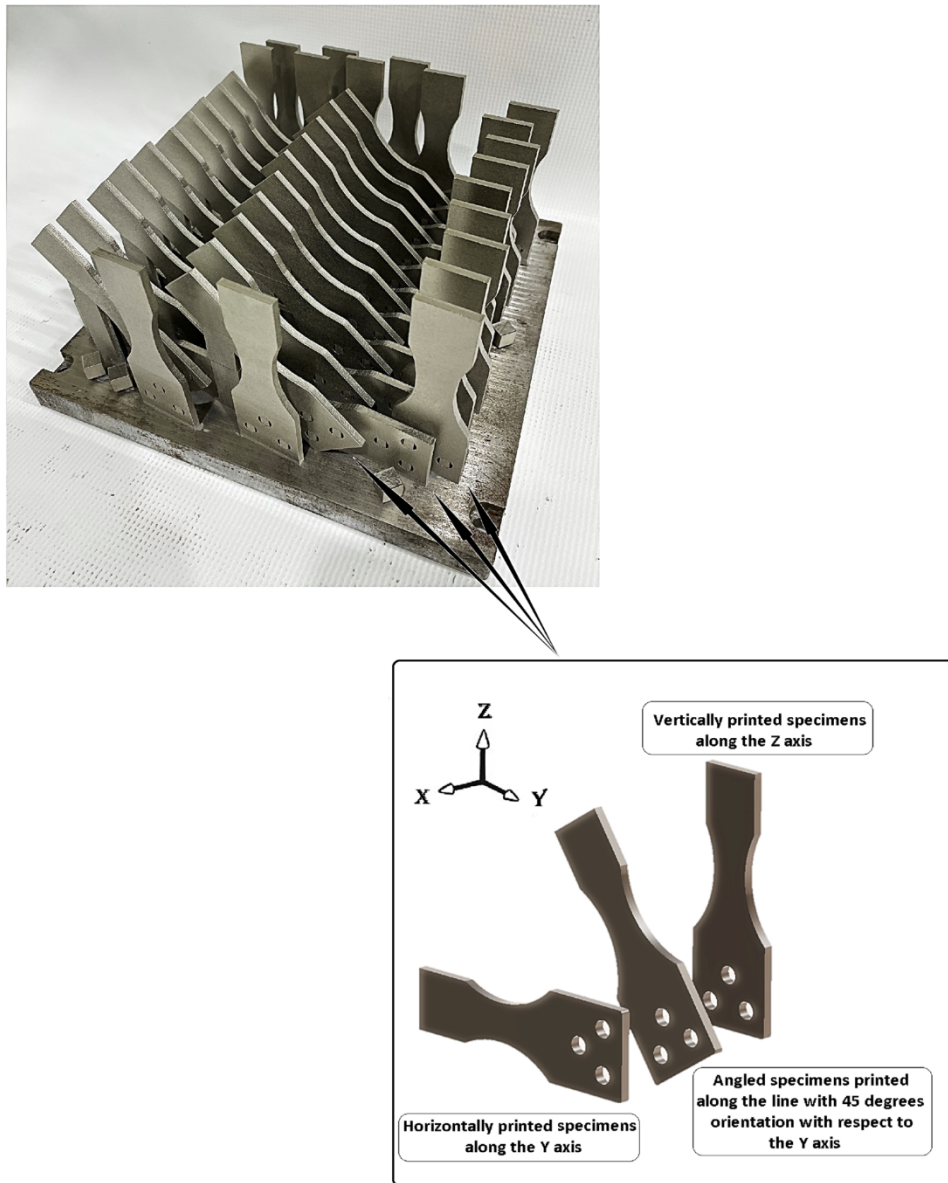
Fig. 2. Printed bending fatigue specimens in 3 orientations of horizontal, vertical, and angled.

Shrestha et al. [23] investigated the effect of build orientation on the fatigue of LB-PBF stainless steel 316 L specimens. They found the diagonally-printed specimens to have the shortest, the horizontally printed the longest fatigue life, and vertically-printed specimens having moderate fatigue performance compared to the other two directions. Such findings may be due to a more pronounced influence of elongated defects' alignment with the direction of maximum shear (45° angle with respect to the specimen's longitudinal axis in case of uniaxial loading). It is also suggested that the manner in which the build orientation affects the fatigue performance may also be a function of the loading type and the life regime (the influence of build orientation on fatigue performance is reported to become less pronounced in longer life regimes) [23, 24].

The focus of this paper is on Inconel 718. AM nickel-based alloys and particularly Inconel 718 have been the subject of study in several articles due to their high strength and corrosion resistance, which makes them suitable for operating in extreme environments such as aircraft engines, gas turbines, and powerplant-related facilities [25,26]. Yoo et al. [27] studied LB-PBF specimens of Inconel 718 processed with two different heat treatments via digital image correlation techniques to investigate the locations of strain localization under fatigue. They observed that in stress-relieved specimens, sub-granular cell structures impede the dislocation movements, and this results in the even distribution of micro-strain across the microstructure. On the contrary, no cell boundaries were present in the post-processed specimens, causing strain localization inside or near the grain boundaries. Similar homogenizing effect of the as-solidified cellular structure on strain distribution has recently been shown in Hastelloy X [28]. Gribbin et al. [29] compared the low-cycle fatigue (LCF) performance of three different Inconel 718 specimens in the form of LB-PBF, hot isostatic pressed (HIPed), and wrought. They reported that the LB-PBF Inconel had superior fatigue performance compared to the others.

The energy associated with cyclic slip irreversibility or plastic strain energy is commonly introduced as a reliable parameter for representing fatigue damage at micro, meso, and macro scales [2]. It is important to consider that in cases where the manufacturing defects do not act as crack initiation sites, they may still contribute to increasing the accumulative plastic strain energy by the stress/strain concentration they create. Prithivirajan and Sangid [30] put forward a fatigue life and crack initiation location prediction scheme using the crystal plasticity finite
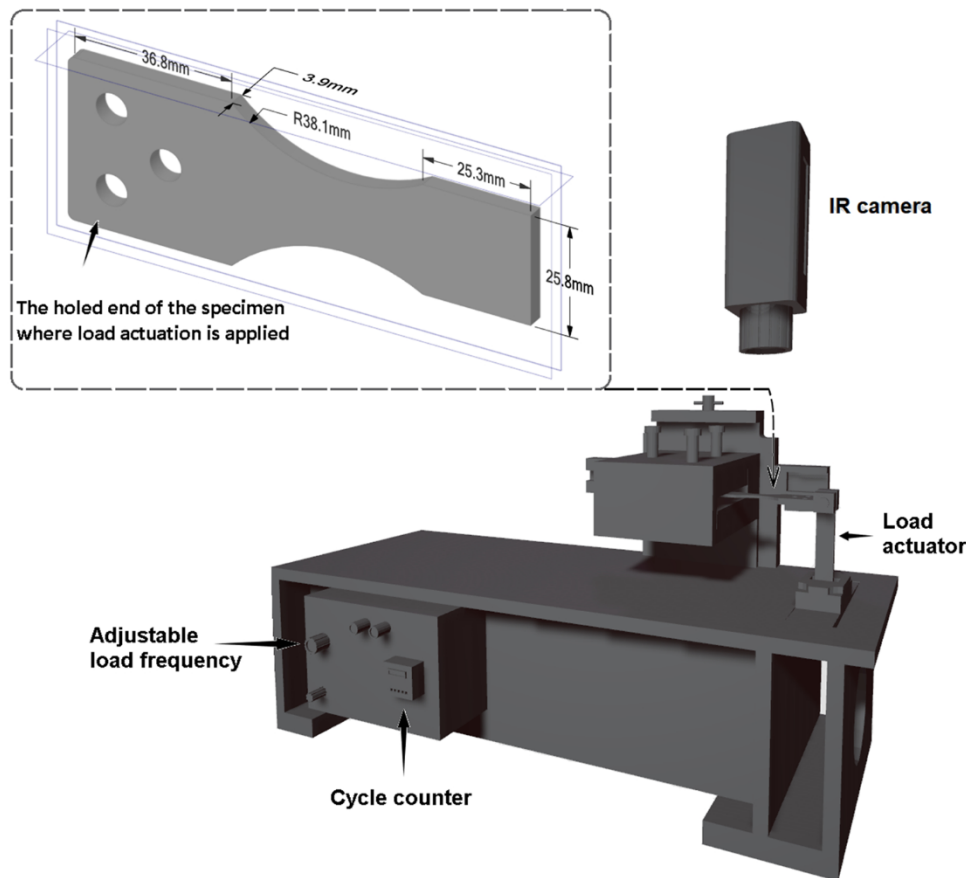
Fig. 3. Bending fatigue tester and the specimen design used to conduct the fatigue experiments in this study.
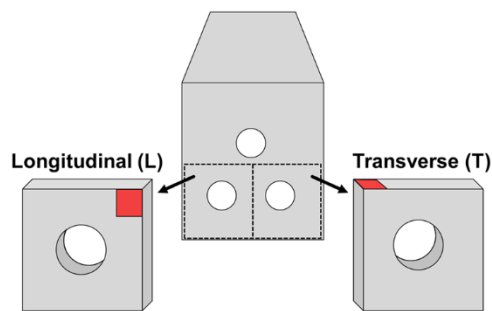

Fig. 4. Schematic illustration of excision performed on the failed bending specimens to produce the microstructural samples.

element method (CPFEM) simulations and included the role of manufacturing pores. Prithivirajan and Sangid used plastic strain energy density as the fatigue damage indicator in their analysis. Chen et al.[31] and Wilson et al. [32] used locally-stored strain energy with integrated crystal plasticity eXtended Finite Element Method (CPXFEM) and successfully predicted the fatigue initiation behavior and crack path/ growth in specimens with BCC, FCC, and HCP crystal structures. Macro-scale methods such as thermography, in essence, consider the manifestation of plastic strain energy in the form of heat dissipation as a measure of fatigue damage [33–35]. Such an approach facilitates their application and gives them the ability to be integrated with microstructure-sensitive algorithms. Jirandehi and Khonsari [36,37] presented a thermodynamic-based and microstructure-sensitive algorithm to predict the fatigue life of metals. They used a Weibull probability distribution function which represents the statistical distribution of cyclic plastic micro-strains based on the stress-strain data from a monotonic tensile test.

The current study implements the microstructure-sensitive algorithm by Jirandehi and Khonsari and a macro-scale thermography-based method to assess the fatigue damage and life in LB-PBF Inconel 718 specimens with different build orientations. In addition, the Impulse Excitation Technique (IET) is used to investigate the defects content in the specimens. In Section 2, the theory of the methods used in the study is elaborated on. In Section 3, the experimental set-ups, including the mechanical, fatigue, IET testers, and the specimens manufacturing details, are provided. Section 4 explains the Finite Element Analysis (FEA) performed to obtain surface temperature distribution under cyclic loading. Finally, Section 5 presents the results and relevant discussions, and Section 6 delivers the conclusive remarks.

2. Methods

In this section, the fundamentals for assessing the overall density of microstructural defects in each printing direction are discussed. For this purpose, the impulse excitation technique is used to measure the structural damping coefficient. Then the plastic strain energy—a measure of the damage caused by the defects under cyclic loading—is explained based on two microstructure-based and macro-scale methods. Finally, the relevant equations for the thermodynamically-based measure known as the Fracture Fatigue Entropy (FFE) for fatigue life estimation are presented.

2.1. Structural damping

Crystallographic and manufacturing defects are the sites where localized plastic deformation occurs, leading to the formation of cracks and eventual failure [9]. Thus, the assessment of the defect content is
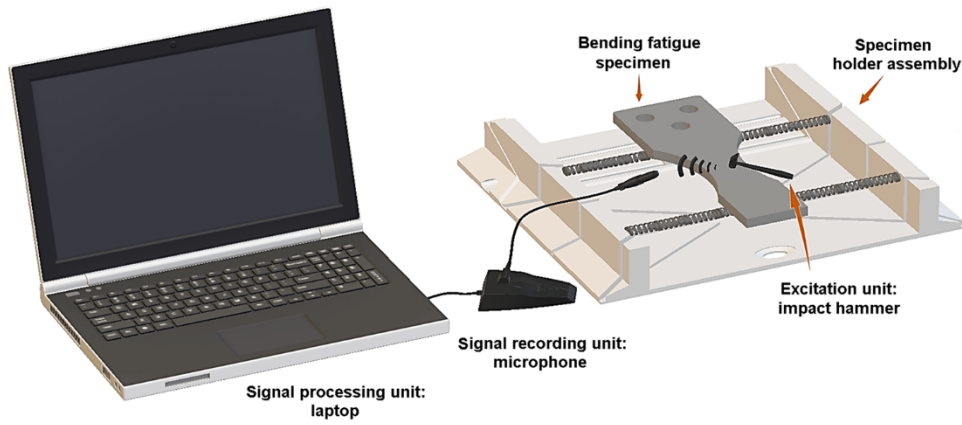
Fig. 5. The RFDA set up used in this study to measure the damping coefficients.
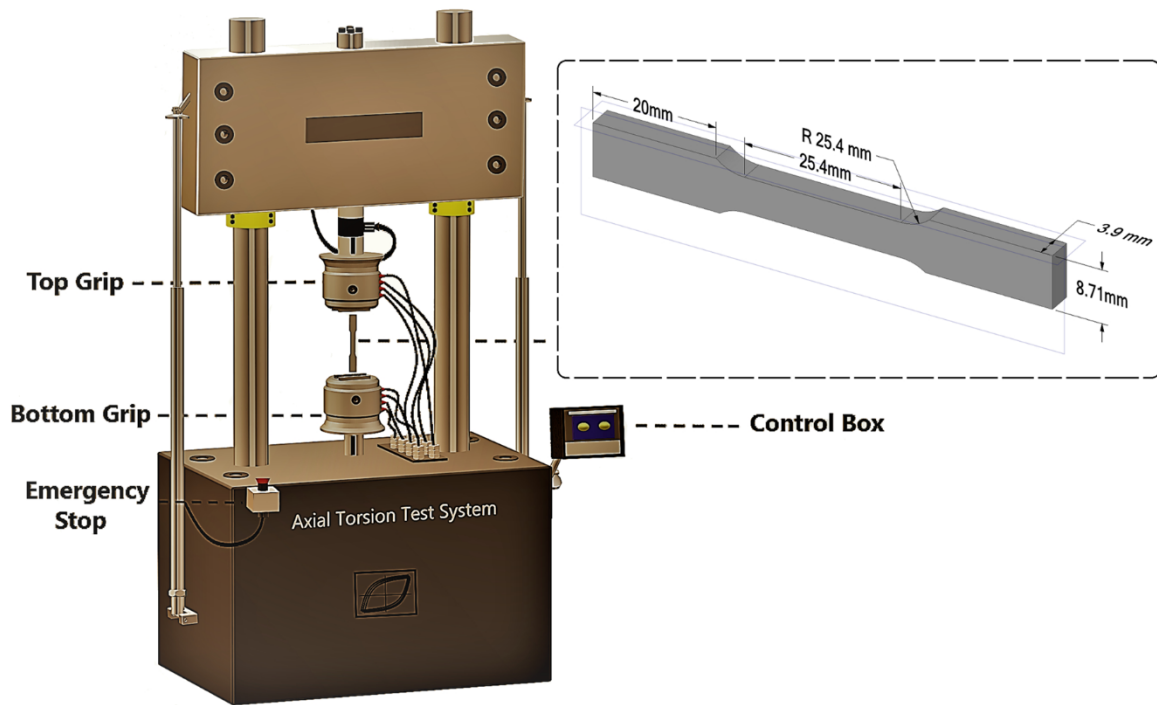

Fig. 6. The mechanical tester used to conduct monotonic tensile tests and the specimen designed in accordance with ASTM standard.

vital in the study of cyclic fatigue. The population of microstructural defects content in a metal's microstructure can be represented by its damping coefficient in response to forced excitation [38,39]. In other words, the microstructural defects act as obstacles that attenuate the excitation wave, and the larger their population, the higher the damping coefficient value. Thus, measurements of the damping coefficient provide useful information on the defect density in specimens printed at different orientations.

Among the three different types of damping—structural, material, and fluid damping—material damping is considered a material property [38]. Damping can be obtained either in the frequency domain by the so-called half-power bandwidth or in the time domain using the exponential free decay curve [40]. While the damping of a pristine material is independent of its geometry, it changes upon experiencing cyclic loading. The change in the damping behavior is a function of the applied stress [41], temperature [42], and frequency [43]. The first theoretical evaluation of damping was pioneered by Zener [44], who defined damping loss or loss factor Q^{-1} as follows (Q is sometime referred to as the quality factor):

$$Q^{-1} = \frac{\Delta E}{2\pi E} \qquad (1)$$

where E is the average energy of vibration during a cycle, ΔE is the energy dissipated per cycle and the ratio $\Delta E/E$ gives a measure of the damping capacity of the solid. Orban [45] defined damping as the conversion of mechanical energy of vibration into thermal energy and suggested that the absorbed energy per cycle can be determined using Eqs. (2 and 3) as follows.

$$D = \oint \sigma d\epsilon \qquad (2)$$

where σ is the stress level, and ϵ denotes the associated strain. Then, having the stored energy U within the loading sequence, one can obtain the so-called *specific damping coefficient* as:
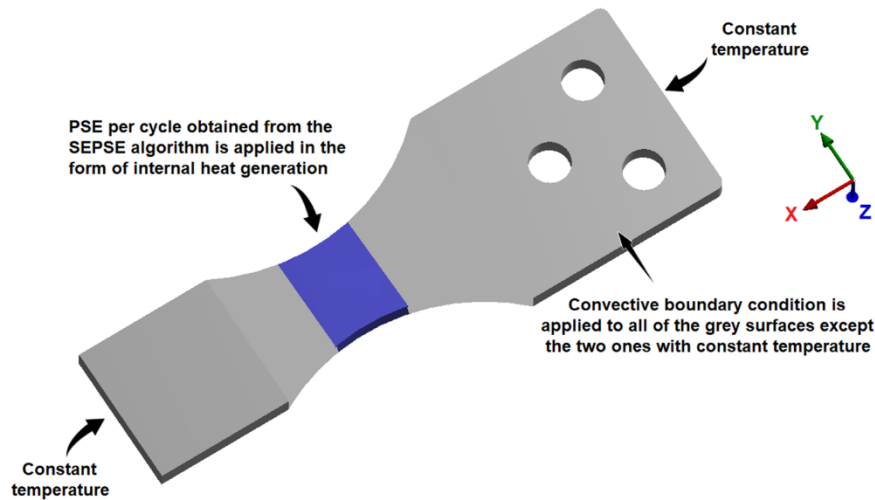
$$\Psi = \frac{D}{U} \qquad (3)$$

Fig. 7. The finite element model of the bending fatigue specimens used in this study.
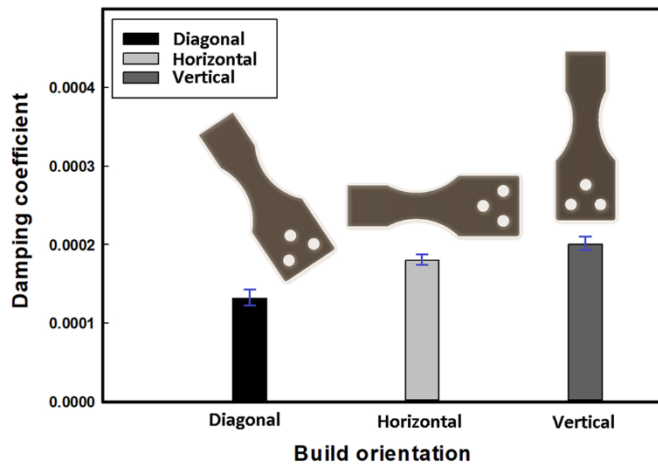

Fig. 8. The damping coefficients of pristine specimens measured via IET for different build orientations.

Given that the plastic strain energy during the cyclic loading is due to plastic deformations, the area captured within the hysteresis loop is needed to evaluate the damping parameter using Orban's approach (Eq. 2). Alternatively, damping can be defined as the loss factor (also known as the damping factor) η, which is the ratio of the energy dissipated per cycle and the maximum elastic energy as follows.

$$\eta = \frac{\Delta E}{2\pi U_{max}} \qquad (4)$$

where U_{max} and ΔE are the maximum elastic energy and energy dissipated per cycle, respectively.

In this paper, we refer to Ψ as the damping coefficient. The relationship among different definitions of damping is summarized in Table 1 [46]. To measure the damping coefficient of the pristine specimens in this study however, the experimental setup explained in Section 3.2 is used. In this method the decay rate of the acoustic feedback wave from a forced excitation signal is merely measured with the device's software.

2.2. Plastic strain energy

Microstructural changes under cyclic loading result in lasting micro-deformations that contribute to fatigue damage. Upon loading, dislocations tend to multiply, move, or get pinned if they face obstacles such as grain boundaries or precipitates. As loading continues, accumulated dislocations in the form of veins collapse and form the ladder-like structures—i.e., persistent slip bands (PSBs)—along the most energetically favorable slip system, known to be the site for the localization of cyclic slip irreversibility or plastic strains. Thus, the work or energy associated with the permanent deformations or plastic strain energy (PSE) may well represent fatigue damage [2].

Crystallographic defects (point, line, planar, volume/bulk) and Manufacturing defects such as pores, keyholes, and lack-of-fusion defects (LOF), can either directly induce crack initiation or contribute to damage initiation/growth by the strong stress/strain field around them [3]. This influence on the strain field across the microstructure leads to an inhomogeneous strain distribution in microscale. It is also shown that the distribution of the plastic micro-deformations under cyclic loading can be represented by a Weibull probability function [2,36,47,48]. Using this concept, Jirandehi and Khonsari [36,37] developed a microstructure-sensitive algorithm for quantifying fatigue damage and estimating fatigue life where the PSE per cycle of material at the desired load amplitude can be estimated by conducting a monotonic tensile test.

The statistical estimation of plastic strain energy (SEPSE) method assumes a polycrystalline material's microstructure in the form of fictitious microelements that undergo different levels of plastic deformations due to the difference in elastic constants, orientation, and proximity with manufacturing defects [36] (Note that the elements discussed in the original work were merely to illustrate the physics for the introduced derivation and are not part of the methodology). Accordingly, it incorporates the heterogeneous behavior of microstructure under cyclic loading by assigning different cyclic plastic micro-strains to the microelements. A two-parameter Weibull probability function $(f(\varepsilon))$ is used to represent the distribution of cyclic micro-strains. Research shows that the cyclic micro stress-strain datapoints experienced by each of the elements follows a similar distribution as in a monotonic tensile test [48,49] and thus may be obtained from a monotonic tensile test at around a stress level equal to the fatigue test's cyclic stress amplitude [47]. Hence, the cyclic plastic micro-strain energy of one element can be expressed in the form of Eq. (5) [36].

$$dE = 2\sigma f(\varepsilon_p)d\varepsilon_p = 2K\varepsilon_p^n \underbrace{\frac{\overbrace{\alpha \times std}^{\text{Weibull shape parameter}}}{\underbrace{\mu}_{\text{Weibull scale parameter}}}}_{} \left(\frac{\varepsilon_p}{\mu}\right)^{\alpha \times std - 1} e^{-\left(\frac{\varepsilon_p}{\mu}\right)^{\alpha \times std}} d\varepsilon_p \qquad (5)$$

where K is the strain hardening coefficient, n is the strain hardening exponent, μ is the average of the strain datapoints from a monotonic tensile test (which in conjunction with the Weibull function represent
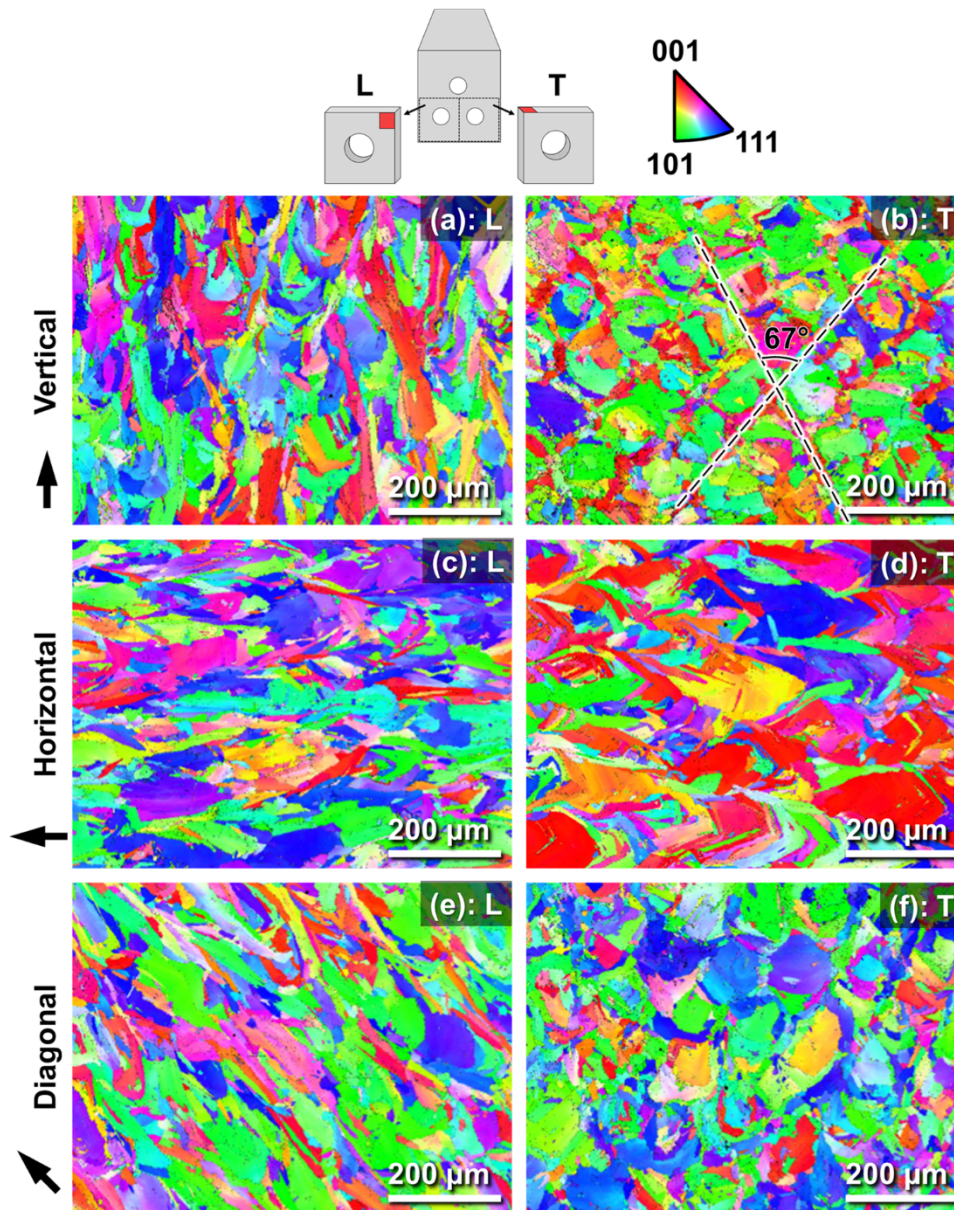
Fig. 9. Inverse pole figure (IPF) maps representing the microstructure on the longitudinal (L) and transverse (T) planes of the specimens. The colors indicate the crystallographic orientations along the normal of the planes where the maps were taken. The arrows indicate the build orientations with respect to the longitudinal planes.

Table 3
The mechanical properties of the IN 718 used in this study with different build orientations.

Build orientation	True yield stress (MPa)	Ultimate stress (MPa)
Diagonal	775	1127
Horizontal	710	1023
Vertical	670	948

the distribution of cyclic micro-strains), and the Weibull shape parameter is defined as a multiplier of the standard deviation of the strain data. Eq. (5) considers the frequency of deformation in any orientation in a randomly oriented polycrystal. According to Esin and Jones [47], $f(s) = $

$\sum_{i=1}^{5} \frac{1}{2s-(i-1)}$ considers the least number of activated slip systems (s) necessary for deformation, preserving material's continuity and satisfying the principal of virtual work at the grain level as put forward by Taylor [50] and Bishop and Hill [51,52]. Additionally, Eq. (5) can be rewritten in integral form within the limits of the true yield point and the assigned strain data point from the monotonic tensile test to consider the plastic deformation of one element. In the SEPSE algorithm the true yield point is defined as the point where the stress-strain curve turns nonlinear (as illustrated and discussed later by Fig. 10). After summing the contribution of all the elements, the PSE per cycle can be expressed in the form of Eq. (6).
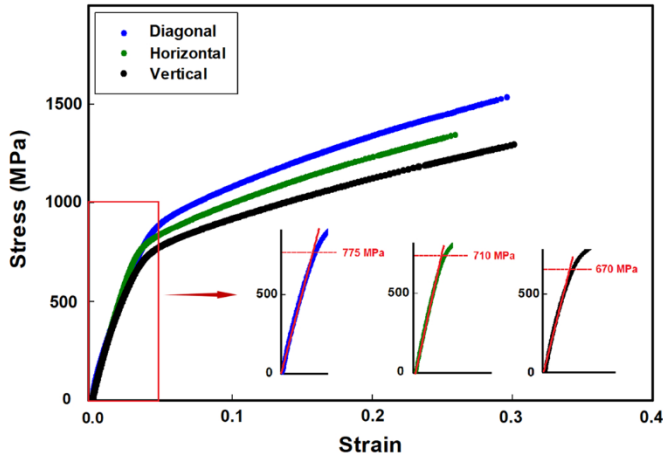
Fig. 10. The true stress-strain curves of the three printing directions used in this study.
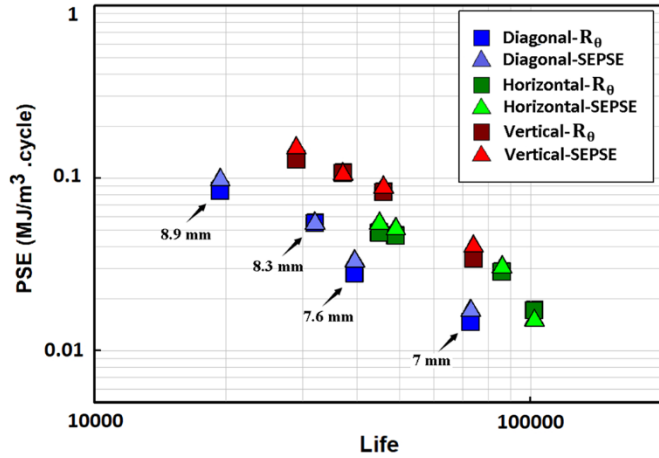

Fig. 11. The plastic strain energy values obtained for each of the printing directions at different applied displacement amplitudes.
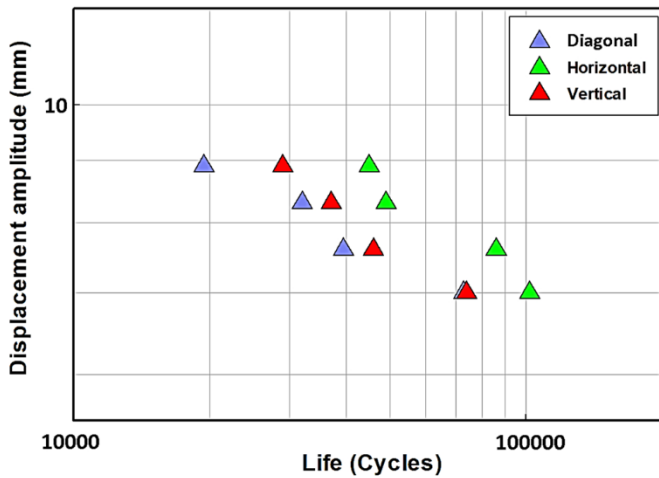

Fig. 12. The displacement vs life curve for the three build orientations.

$$W_{SEPSE} = \sum_{j=1}^{k} 2 \; K \frac{\alpha \times std}{\mu^{\alpha \times std}} \left(\sum_{i=1}^{5} \frac{1}{2s - (i-1)} \right) \int_{Y}^{\epsilon_k} \varepsilon_p^{n+\alpha \times std - 1} \; e^{-\left(\varepsilon_p/\mu\right)^{\alpha \times std}} \; d\varepsilon_p$$

(6)

where ϵ_k is the strain data points from the neighboring points of the analyzed stress level (cyclic test stress amplitude) on the monotonic tensile stress-strain curve which are weighted with the integral of the Weibull probability density function. The estimated PSE based on the Eq. (6) is fairly sensitive to the α parameter or the multiplier of the standard deviation. The complete procedure for finding the right α value is explained in [36]. Briefly, it was found that a proper choice of α may be obtained according to the point where $\frac{\partial^2 PSE}{\partial \alpha^2} = 0$ [36,37]. In other words, by assigning different values of α numerically, the variation of PSE has to be plotted first. Then, the point where the convexity changes direction is an indication of the proper α value (See Fig. 1). It may also be considered that for a chosen α value the peak of the Weibull distribution on the monotonic stress-strain curve—which is also the micro-strain value that the majority of elements experience— needs to be approximately the same as the cyclic macro-strain the corresponds to the applied remote cyclic load amplitude (See Fig. 1).

In macro-scale, the cyclic damage or cyclic plastic work primarily manifests in the form of dissipated heat. Measuring a material's surface temperature during a fatigue test to obtain the dissipated heat is extensively reported in the literature [53–58]. The surface temperature evolution under cyclic loading follows three stages. In Stage I, there is a rapid increase during a short period of time. Subsequently, the temperature nearly reaches a steady-state in stage II, and most of the fatigue life is spent here. Lastly, the specimen temperature rapidly rises at stage III, which leads to failure. Amiri and Khonsari [59] showed the slope of the temperature evolution curve early stage I can be used as a parameter for measuring the PSE per cycle using the following equation (known as the R_θ method).

$$\dot{w}_p = \rho c_p R_\theta|_{t=0}$$

(7)

where $\dot{w}_p$ is the PSE rate, ρ is the density, c_p is the specific heat capacity and R_θ is the initial slop of temperature at $t = 0$. Jang and Khonsari [60] have shown that using the initial slope of temperature ($R_\theta|_{t=0}$) to calculate the PSE, yields identical results to the method put forward by Meneghetti et al. [61] (the method used by Meneghetti uses the slope of the cooling curve at mid-life after stopping the test).

2.3. Fatigue fracture entropy (FFE)

The generated heat due to cyclic loading contributes to increasing the specimen's surface temperature through plastic deformations ($\sigma : \dot{\varepsilon}^p$, which is convected to the surroundings), and heat conduction in the specimen ($k\nabla^2 T$). Considering the conservation of energy principle, the heat transfer equation can be expressed as in Eq. (8) in general tensorial from.

$$\rho C \dot{T} = \sigma : \dot{\varepsilon}^p \quad + k\nabla^2 T$$

(8)

One can use the Clasius-Duhem inequality ($\rho \frac{\partial S}{\partial t} + \nabla.(\frac{\vec{q}}{T}) \geq 0$) or the second law of thermodynamics to arrive at the volumetric entropy generation rate ($\dot{\gamma} = \frac{\sigma : \dot{\varepsilon}_p}{T} - \frac{A_k \dot{V}_k}{T} - \frac{k\nabla^2 T}{T^2} \geq 0$) [62]. Since the dissipated heat due to plastic work outweighs the two other terms, the entropy accumulation until the failure of a specimen can be obtained via Eq. (9). Naderi et al. [62] postulated that this accumulation of entropy—introduced as FFE— is a material property, independent of the geometry, load, and test frequency. Once the FFE of a material is known, it can be used to estimate the fatigue life of the material for desired stress levels using a micro-scale approach (SEPSE-Eq. 6) [37] or a macro scale methodology (R_θ-Eq. 7)[59].

$$FFE = \int_0^{t_f} \dot{\gamma} \; dt = \int_0^{t_f} \frac{\dot{w}_p}{T} dt$$

(9)

Given that the majority of fatigue life is spent in the stage II of temperature evolution curve Eq. (9) can be expressed in the following
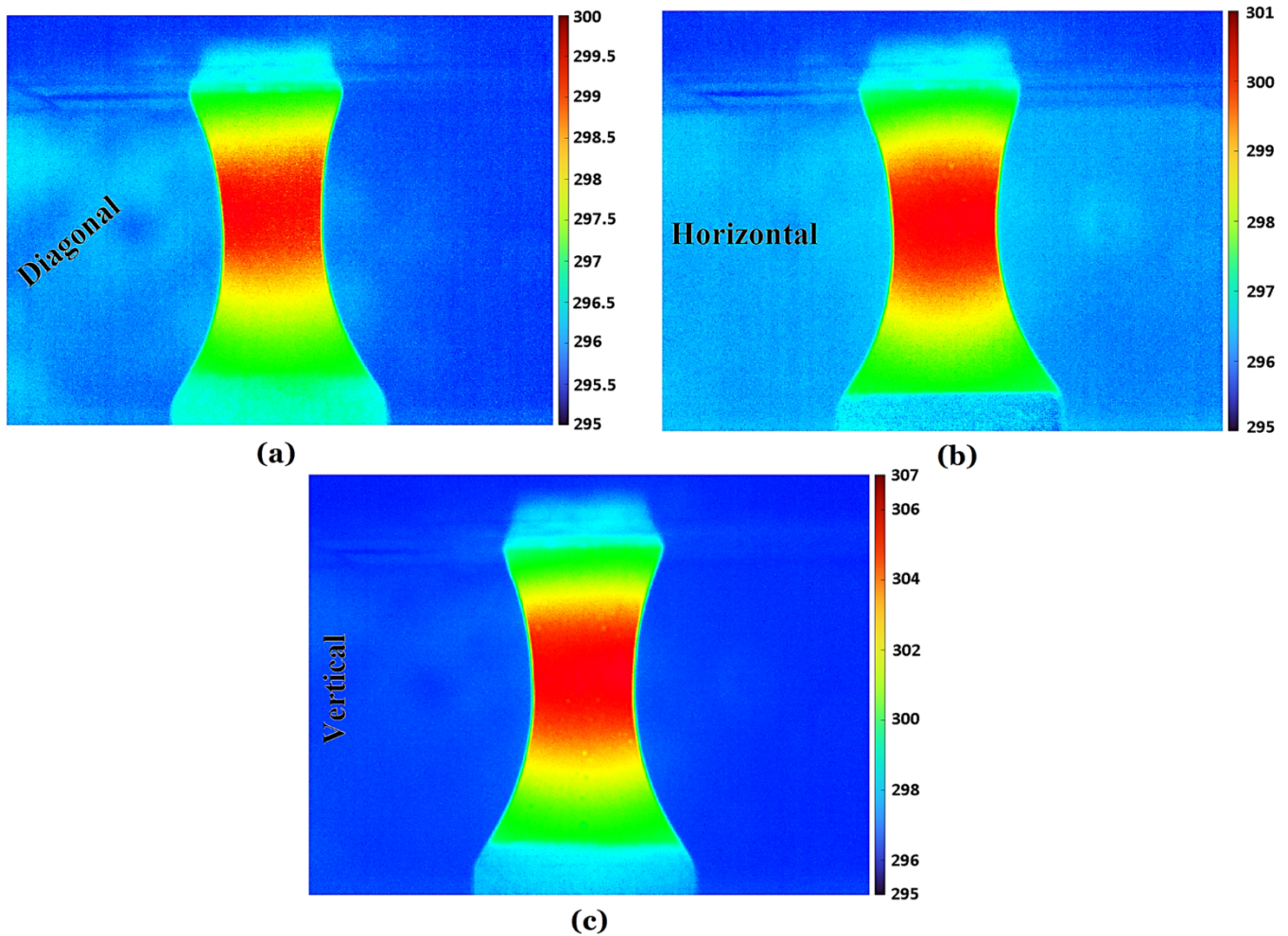
Fig. 13. The distribution of steady-state temperature (K) at 7 mm displacement amplitude via the IR camera measurements for a) the angled specimen b) horizontally-printed specimen c) vertically-printed specimen.

form [37].

$$\text{FFE} = \frac{N_f * \dot{w}_p}{T_{ss}} \tag{10}$$

where N_f is the number of cycles to failure, and T_{ss} is the steady-state temperature in stage II of temperature evolution curve.

3. Experimental

3.1. Material and additive manufacturing process

Gas-atomized Inconel 718 powder (Carpenter Additive, UK) is used and processed by the EOS M290 system—an LB-PBF platform. The EOS-recommended laser scan speed, power, and other process parameters used this work are listed in Table 2. No additional optimization was performed to ensure that the results generated are relevant for most AM practitioners at large.

Three orientations of specimens were printed as shown in Fig. 2. The vertically-printed specimens were built upright, meaning the angle between the specimen's longitudinal axis and the printing substrate was 90°. In contrast, the longitudinal axis for the horizontally-printed samples was parallel to the substrate (zero-degree orientation). The diagonally-printed (angled) specimens' axis was angled 45° with respect to the substrate. It is worthwhile to point out that the test specimen designs, as explained in Section 3.2, were fabricated into net shapes.

From among the numerous advantages, additive manufacturing technology lends itself to the direct and accurate building of complicated structures, parts and design which require operating in various work conditions. Since it is important to make quality products with such processes with the least amount of post-processing the specimens in this study have received no heat treatment (HT). The results presented in this paper provide a benchmark for non-heat treated /polished specimens. Silicon carbide sandpapers with grit numbers— from 400 to 2000—was used to polish each specimen's gauge section and ensure that the surface roughness is eliminated and does not affect the fatigue results.

3.2. Fatigue tests

Flat dog-bone specimens are designed in accordance with the ASTM-STP566 as indicated in Fig. 3. The bending fatigue specimens are manufactured for use in cantilever fully reversed-bending tests ($R = -1$) with tapered widths proportioned to produce nominally constant stress along the test section. The specimens' corners—where there were residues after cutting the specimens off from the printing substrate—were machined and then all the surfaces were polished using sandpapers with grit numbers starting from 400 to 3000 to obtain a surface finish with a maximum surface roughness of 2 μm based on the ASTM standard, to eliminate the effect of manufacturing surface roughness as a potential site of fatigue crack initiation (FCI). A schematic of the experimental setup for the cyclic bending test is presented in Fig. 3. The apparatus is a compact bench-mounted unit with a variable throw crank
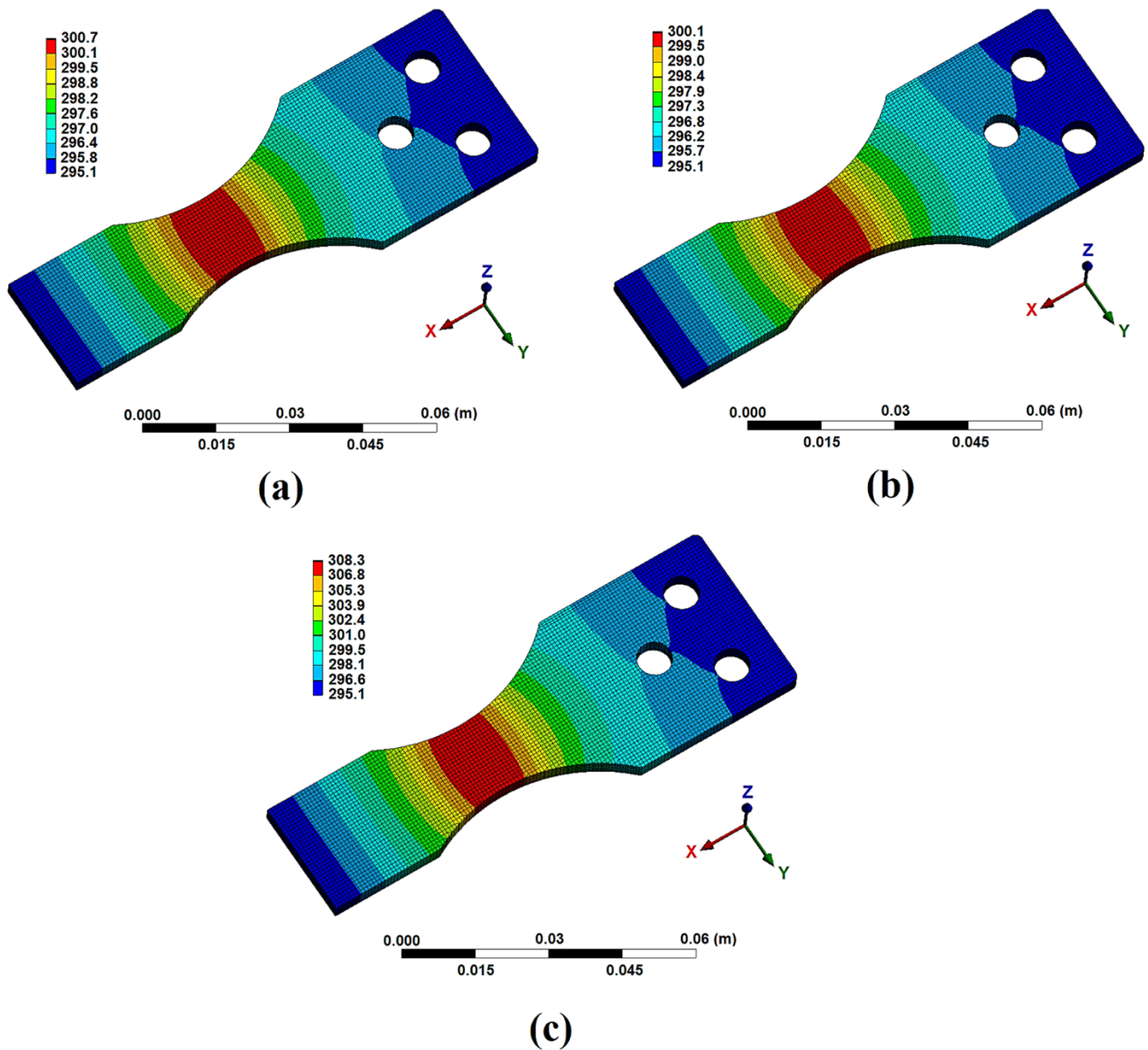
Fig. 14. The distribution of steady-state temperature (K) at 7 mm displacement amplitude via the FEM for a) the angled specimen b) horizontally-printed specimen c) vertically-printed specimen.

(adjustable from 0 to 50 millimeters), a variable-speed motor connected to the reciprocating platen, with a failure cut-off circuit, and a cycle counter. Tests involved bending fatigue of a specimen clamped into the machine at one end and actuated cyclically at the other end at desired amplitude and frequency. At least two specimens were tested for one load amplitude and printing direction (in case the failure lives were not very close a third test was conducted to ensure a proper average is reported). It is worthwhile to point out that the tests were continued until the specimens completely break and then the lives were recorded.

A FLIR A615 Thermal Imaging IR Camera with 640 × 480-pixel resolution and 50 mK sensitivity is used to record the surface temperature evolution of the specimen during loading. The camera is capable of recording images up to 200 frames per second using a windowing option. It is mounted with a constant distance of 20 cm over the specimen (See Fig. 3).

3.3. Examination of microstructure and fracture surfaces

A microstructure examination was performed on samples excised from failed specimens at the grips in the regions between the bolt holes. The microstructure at this region is not to be expected by influenced by the bending deformation during the fatigue tests. In addition, during fabrication, this region is relatively far from the heat sink effect of the base plate and its microstructural information should be representative of the gage. Two samples were excised from each specimen of different orientation to reveal microstructure on the longitudinal (L) and the transverse (T) planes (see Fig. 4). After mounting with epoxy, the specimens were ground using sandpapers with reducing grit and was polished with 0.05 µm diameter colloidal silica before vibratory polishing. Colloidal silica of 0.02 µm diameter was used for vibratory polishing for 4 hrs. Electron backscatter diffraction (EBSD) analysis was performed using the Oxford instruments onboard of a Zeiss Crossbeam 550 scanning electron microscope (SEM) to reveal the orientation, size,
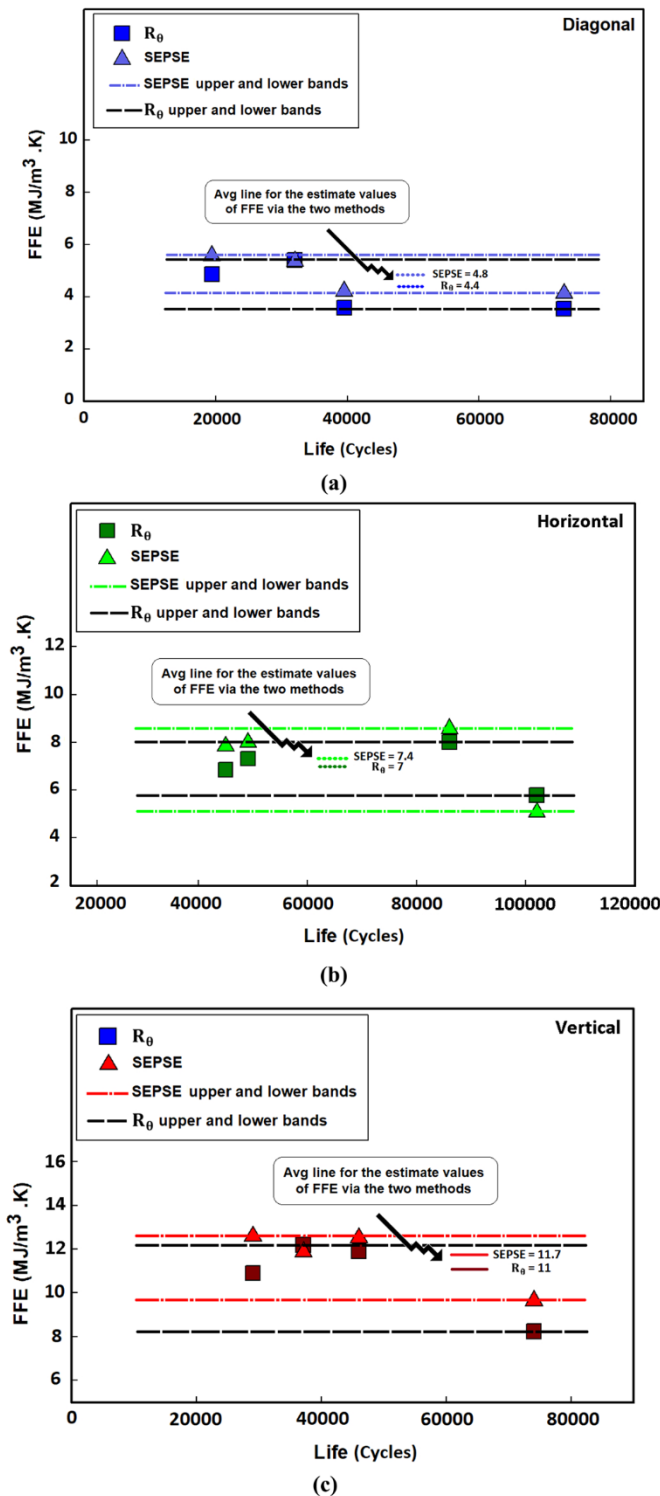
Fig. 15. The FFE of the studied material for all the cases studied a) Diagonal b) Horizontal c) Vertical.

and morphological information of the grains. Fractography was performed in the same microscope.

3.4. Impulse excitation technique (IET)

A resonant frequency domain analysis (RFDA) using an IMCE test set up (Integrated Material Control Engineering Nv-Belgium) is used to measure the damping of a pristine specimen (see Fig. 5 for the test set up). The non-destructive testing device can measure the damping, resonant frequencies, and elastic modulus of a specimen. This instrument uses two supporting parallel strings that provide a free-free vibration mode for the specimen tapped with a ball head hammer to induce vibrational load. In these tests, the impact hammer vertically hits the top surface on gauge section to produce acoustic signals (out-of-plane impact load along the same direction that fatigue bending loads are applied). Then, the commercial software uses logarithmic decrement method to calculate the damping coefficient of the acoustic feedback signal. Since damping is a measure of the energy absorption by the material, it is important to avoid any external vibration to obtain the true response of the specimen to mechanical impulse. Accordingly, the supporting strings, impulse locations, and signal pickup points should be properly selected to induce and measure specific modes of vibration. A series of tests revealed that the damping results are insensitive to the above-mentioned settings when dealing with a pristine specimen. Full details of the apparatus and the experimental procedure is given in [38].

3.5. Monotonic tensile tests

Monotonic tensile test specimens (flat dog bone) are designed and prepared in accordance with the ASTM-E8/E8M standard. A servo-hydraulic fatigue tester (930 series, Test Resources, USA) is used to perform the monotonic tensile tests and obtain the specimen's true stress-strain curves. The machine is capable of applying up to 50 kN axial load and 75 Hz frequency. As shown in Fig. 6, the specimen is placed and gripped in between the bottom and top jaws. During the test, the bottom grip actuates while the top one stays stationary.

4. Numerical

When using macro-scale method (Eq. 7) to obtain PSE and calculate FFE (Eq. 10) an IR camera is used to measure the steady-state temperature. In contrast, the SEPSE-based algorithm uses finite element analysis (FEA) to calculate this temperature value [37]. The ANSYS workbench software environment is used for this purpose, and transient thermal analysis is performed to obtain the steady-state temperature. ANSYS Solid-70 element types are used in this analysis, and a number of 40297 elements was used after performing a mesh-independency analysis. As shown in Fig. 7, the thinnest volumetric portion within the gauge section is used to apply the plastic strain energy rate value in the form of internal heat generation (such consideration is based on observations from the IR camera throughout the experiments, as shown in Fig. 13). The normal surfaces at the ends of the specimen are assigned with a fixed temperature value at room temperature/initial temperature of the specimen (295.15 K) [37]. A convective boundary condition is applied to all the other surfaces where a heat transfer coefficient of 25 $\frac{W}{m^2.K}$ is considered [37].

5. Results and discussion

5.1. Damping analysis

The level of defects in each printing direction were examined via the IE technique. Fig. 8 shows the damping value of the specimens in different build orientations and its scatter across the samples of each direction. Three specimens were tested from each printing direction, and the test was repeated five times for each of the pristine specimens. For one printing direction, the average value from repeating the test for each of the three specimens was recorded. Then, damping values from the three specimens were averaged to obtain the structural damping coefficient of that printing direction. Damping is a measure of how intensely the excitation wave is blocked within the microstructure due to microstructural defects. Therefore, the higher the damping coefficient, the higher the defects contents are. On this account, the vertical build
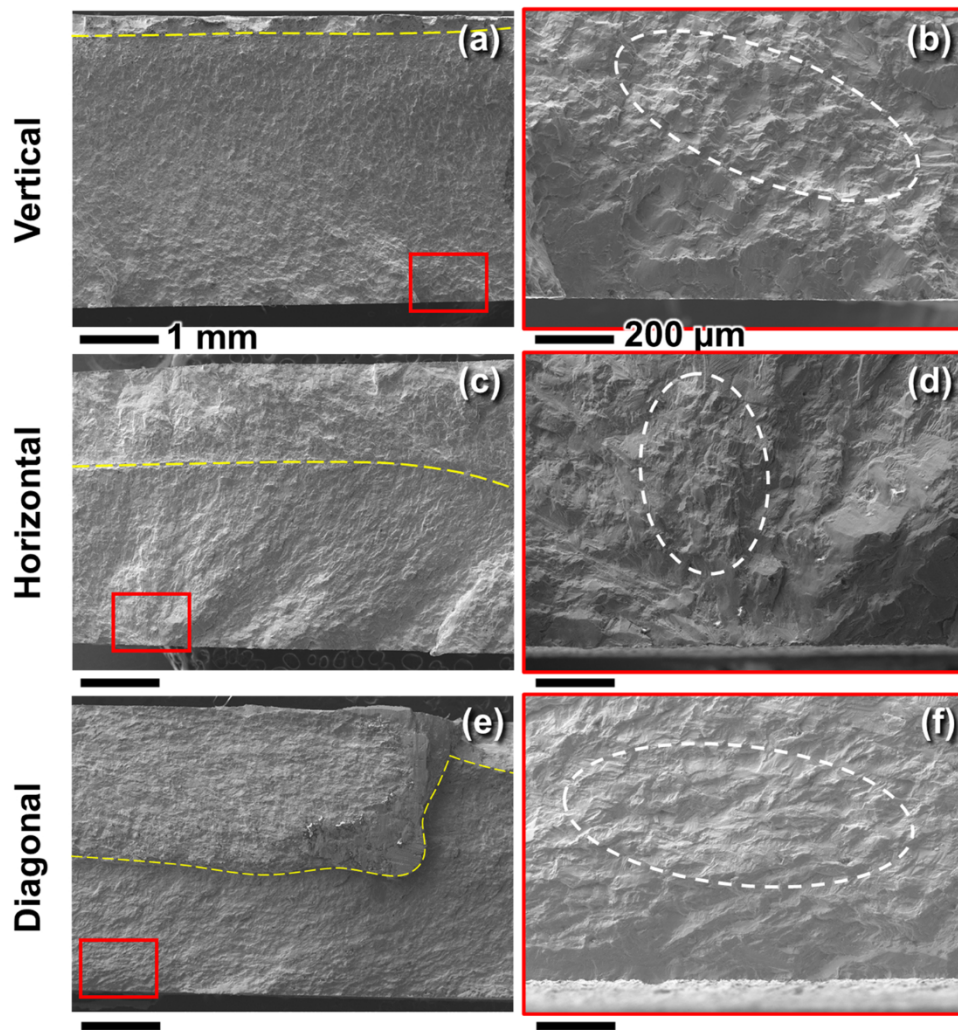
Fig. 16. Fracture surfaces of specimens tested under the lowest stress amplitudes for each build orientation. The yellow dashed lines in (a), (c), and (e) indicated the locations where final fracture occurred. Figures (b), (d), and (f) provide magnified views of the boxed regions shown in (a), (c), and (e).

orientation contains the highest level of defects, while the diagonal specimens contain the least number of defects. It is worth mentioning that this method cannot differentiate between different types of microstructure defects and is just a holistic measure of all the defects of any type inside the material in general. It is also worthwhile to point out that containing more crystallographic or manufacturing defects does not necessarily mean a higher fatigue damage. The defects' size, shape, and orientation as well as the loading regime and environmental conditions play a role. It is important to emphasize that this analysis was performed only on pristine specimens and the results do not necessarily represent the behavior of cyclically-loaded specimens where defects tend to grow and multiply.

5.2. Microstructure analysis

The microstructure, as revealed by the inversed pole figure (IPF) maps, is shown in Fig. 9. As shown, the classical "U" shaped grains are evident on the longitudinal planes for all build orientations with the opening along the build directions (see Figs. 9a, 9c, and 9e). In addition, there is a "tiling" pattern on the transverse plane of the vertically built specimens comprising bigger grains (~100 μm diameter) arranged along two directions that are ~67° apart (see Fig. 9b). This is due to the 67° rotation angle between the hatching direction of adjacent layers and that the melt pools typically penetrate two layers. A tiling pattern, although being less pronounced than the one shown in Fig. 9b, is also

seen on the transverse plane of the horizontally built specimens. This as-solidified microstructure is common in alloys processed with LB-PBF and is observed not only in nickel-based alloys [28] but also in stainless steels [8,63]. The transverse plane of the horizontally built specimen (Fig. 9d) showed a similar "U" shaped grains as the longitudinal plane (Fig. 9c), as both planes contained the build direction. Overall, the grains shown in Figs. 9a, 9c, and 9d are slender and curvy, and lacks the regular occurring larger patches shown in Figs. 9b and 9f.

5.3. Plastic strain energy

Monotonic tensile tests were performed to obtain the mechanical properties and data required for calculating the PSE per cycle at desired cyclic load amplitude via the SEPSE algorithm. In particular, the true stress-strain curve of the material with each printing direction is needed where true stress and strain (σ_t, ε_t) can be obtained based on the obtained engineering stress and strain (σ_e, ε_e) from the monotonic tensile test via $\sigma_t = \sigma_e(1 + \varepsilon_e)$ and $\varepsilon_t = Ln(1 + \varepsilon_e)$. Table 1 lists the true yield stress—the location Table 3 where the stress-strain curve becomes nonlinear (as shown in Fig. 10)— and the ultimate strength values of the material. The true stress-strain curves used for the analysis are presented in Fig. 10.

Fully reversed fatigue bending tests are conducted at four displacement amplitudes of 7, 7.6, 8.3, and 8.9 mm via the fatigue tester shown in Fig. 3. Microstructure-sensitive algorithm (SEPSE) and the macro-scale method (R_θ) in Section 2 –Eqs. 6 and 9, respectively—are used to

obtain the PSE per cycle at different life cycles. With the macro-scale method, the initial slope of the temperature rise at the beginning of each experiment is used to calculate the PSE per cycle (See Section 2.2). In the SEPSE calculations, however, the equivalent stress (von Mises) amplitude of each cyclic test is used to get the micro-strain and stress data from the true stress-strain curves in Fig. 10 and then calculate PSE per cycle based on Eq. (6). Fig. 11 indicates the PSE per cycle values estimated via the SEPSE method for each of the printing directions at different displacement amplitudes. Overall, it can be seen that the vertical orientation produces the maximum amount of fatigue damage or PSE per cycle as compared to the other two orientations. Further, a good agreement between the estimation via the two methods is seen.

The two micro-scale and macro-scale methods in this study are local fatigue damage analysis methods, meaning they estimate the accumulating damage around the approximate region of failure in gauge section (in contrast with the non-local CPFEM methods which consider the damage at the exact crack initiation location/spot [2]). On that note, the methodologies used in this work estimate the contribution of all the crystallographic and manufacturing defects (as potential hotspots) to the amount of measured heat dissipation or calculated PSE per cycle (irrespective of whether they are at the exact spot of final critical crack leading failure). Additionally, in the vertical orientation the defects/grains are mostly elongated along the normal direction to the longitudinal axis of the specimen which leads to high stress concentration at their corners [18]. Considering that the vertical orientation has the highest defects content (based on IET measurements in Fig. 8) and the lowest mechanical strength (Fig. 10), it is logical to see a more significant damage compared to the other two build orientations at the same displacement amplitude. By the same token, the horizontal samples experience less fatigue damage and superior fatigue life. Nonetheless as seen in Fig. 12, the diagonally-printed samples have the shortest fatigue life overall. Such observation can be explained by knowing that the orientation of interlayer defects/grains is along the 45° line with respect to the specimen's longitudinal axis in this case and also given the fact that the microstructurally-small crack initiates in the direction of maximum shear (also 45° with respect to the specimen's longitudinal axis) [6,18].

5.4. Fracture fatigue entropy

In this section, we focus on evaluating the FFE for the three studied printing directions of IN 718. For this purpose, the FE model as explained in the Section 4 is used to obtain the steady state temperature and compared against the experimentally obtained values via the IR camera. Fig. 13 indicates the experimentally measured temperature values for the three printing directions at 7 mm displacement amplitude. Fig. 14 shows the finite element model and the distribution of PSE at 7 mm displacement for each of the three printing directions. It can be seen that the predicted temperature ranges via FEA are close to the experimental values in Fig. 13. Further, when the distribution of the critical temperature around the narrowest part of gauge section is considered, the hottest regions in the experimental and numerical plots agree in size and location. Such observations indicate the reliability of the performed numerical analysis.

Fig. 15 shows the experimental results of FFE—using the IR camera measurements of temperature and the R_θ method as in Eq. (8)— versus the values obtained via the microstructure-sensitive algorithm (where the SEPSE method in Eq. (6) alongside the FE simulations to obtain the midlife temperature). It can be seen that both methods yield different FFE values for different build orientations. This behavior is expected since although the same powder and composition are used, the specimens with different build orientations have different mechanical/fatigue characteristics, as discussed earlier. Regardless, the FFE stays within a narrow band for each of the printing directions. In Fig. 15, the upper/lower estimated FFE limits based on the SEPSE and macroscale methods are indicated via dash-dotted and dashed lines for each

orientation, respectively. Further, the obtained average FFE values via the two micro- and macro-scale methods show less than 10% of error, indicating their reliability.

By having the FFE of each printing direction at this point, one can use Eq. (10) in conjunction with the SEPSE algorithm and FEM simulations of temperature to estimate the fatigue life at desired load amplitudes. For instance, in the case of diagonally-printed specimens and 9.5 mm displacement amplitude, the calculated PSE per cycle via SEPSE is $1.86 \times 10^5 \frac{J}{m^3.cycle}$. Using FEA the steady-state is 354 K. Accordingly, the predicted fatigue life is 10,100 cycles. The experimental life is found to be 10,600 cycles, indicating that prediction had an error of 4.7% error. Another example is the case of horizontally-printed samples at 6.35 mm displacement amplitude, where the PSE per cycle is estimated to be $1.27 \times 10^4 \frac{J}{m^3.cycle}$. When the FEA is used, the mid-life temperature for this case is 299.3 K, and using Eq. (10) the predicted fatigue life is 174,100. In comparison with the experimental life of 156000 cycles, the error of estimation for this case is 11.6%. These examples indicate the reliability of the utilized microstructure-sensitive algorithm for quantifying fatigue damage and assessing fatigue life.

Although PSE per cycle is a preliminary measure of the amount of fatigue damage occurred in one cycle, the FFE represents fatigue damage at a much broader time frame—i.e. until its failure. Based on the Eq. (10) the amount of entropy produced in material is mainly dependent on the accumulation of plastic strain energy over the life span of a specimen [37]. The vertically printed samples—lowest mechanical strength and highest defects content—contain the highest PSE per cycle which keeps accumulating over an intermediate life span (as compared to the other two orientations). Hence, they produce the highest accumulated entropy/damage until failure. The horizontal samples, however, produce almost the same scale of plastic damage per cycle compared to the diagonal specimens but for a much larger life span than both of the other orientations. Hence, the total accumulated entropy until their failure is larger than the diagonal specimens. Considering that the horizontal samples have a better overall fatigue life and an intermediate entropy index, they may be considered as the suggested orientation.

5.5. Fractography

Fracture surfaces (as shown in Fig. 16) indicate that the fatigue cracks on each specimen initiated from the two surfaces where the bending stresses were maximum. However, the growth rates of cracks from both sides of the specimens were not equal, which lead to asymmetric features on the fracture surfaces. Note that the yellow dashed lines indicate the location where the major cracks from both sides of the specimens met and induced final fracture. Along the "top" and "bottom" edges of the fracture surfaces shown in Figs. (a), (c), and (e), where the bending stresses were the maximum, the fatigue cracks were seen to have initiated at multiple locations simultaneously. These features are consistent with the well-known fracture surface features of square-gaged specimens under reversed bending [64]. Interestingly, none of crack initiations were *originated* from manufacturing defects (such as pores, keyholes, or lack-of-fusion defect). Magnified views of typical crack initiation sites of the fractured specimens of different build orientations were shown in (b), (d), and (f). Regions near the top and bottom edges of the fracture surfaces, where the crack initiation size resided, were damaged due to contact between fracture surfaces during loading. Nevertheless, regions immediately inside the fracture surfaces (such as the ones enclosed by the dashed lines) clearly contain crystallographic facets. This indicates that the cracks were initiated from crystallographic features, most probably PSBs [7], which formed facets. The size and morphology of these facets resemble those of the grains shown on the transverse planes in Fig. 9.

6. Summary and conclusions

The fatigue degradation of additively manufactured Inconel 718 parts with no heat treatment in vertical, horizontal and diagonal build orientations is assessed via two microstructure-sensitive and macro-scale methods. The macro-scale method uses the initial slope of temperature rise to estimate PSE per cycle. The microstructure-sensitive algorithm, however, is based on the distribution of cyclic micro-plastic deformations. Impact excitation analysis via damping coefficient measurements area was performed to analyze the defects contents at different build orientations. Based on the damping measurements, the vertical build orientation had the highest level of porosity. The highest overall level of fatigue damage (PSE) at this build orientation compared to the other build orientations supports the measured damping results.

Finite element analysis and IR camera measurements of the surface temperature are used to calculate the FFE of material at each build orientation. Each printing direction was shown to have a particular FFE. The FFE for the vertically-printed samples was $FFE_{avg\text{-}SEPSE}= 11.7 \pm 1.5$ $\frac{MJ}{m^3.K}$ versus $FFE_{avg\text{-}R\theta}= 11 \pm 2 \frac{MJ}{m^3.K}$, for horizontally-printed specimens $FFE_{avg\text{-}SEPSE}= 7.4 \pm 1.7 \frac{MJ}{m^3.K}$ versus $FFE_{avg\text{-}R\theta}= 7 \pm 1.1 \frac{MJ}{m^3.K}$, and for the diagonally-printed ones, it was $FFE_{avg\text{-}SEPSE}= 4.8 \pm 0.7 \frac{MJ}{m^3.K}$ versus $FFE_{avg\text{-}R\theta} = 4.4 \pm 0.9 \frac{MJ}{m^3.K}$. Such numbers indicate the FFE for a particular build orientation stays within a narrow band, and a fracture can be considered when the average FFE value is surpassed. Accordingly, the horizontal build orientation is suggested as the preferred orientation—non-heat treated and polished samples— due to its higher fatigue life and moderate level of total accumulated fatigue damage based on the FFE index (slightly higher than the diagonal orientation). The obtained FFE values can be used to estimate fatigue lives for these orientations tested at arbitrary load amplitudes via the microstructure-sensitive algorithm. This study further indicates the reliability of the recently developed microstructure-sensitive algorithm for predicting the fatigue life of AM materials.

CRediT authorship contribution statement

Arash P. Jirandehi: Writing – original draft, Investigation, Software. **Patricio Carrion:** Investigation. **Nima Shamsaei:** Writing – review & editing. **Shuai Shao:** Writing – review & editing, Investigation, Funding acquisition. **Behnam Hajshirmohammadi:** Investigation. **Michael Khonsari:** Investigation, review & editing, Funding acquisition.

Declaration of Competing Interest

The authors declare that they have no known competing financial interests or personal relationships that could have appeared to influence the work reported in this paper.

Acknowledgements

Disclaimer

References

[1] M. Gorelik, Additive manufacturing in the context of structural integrity, Int. J. Fatigue 94 (2017) 168–177.

[2] A.P. Jirandehi, M.M. Khonsari, General quantification of fatigue damage with provision for microstructure: a review, Fatigue Fract. Eng. Mater. Struct. 44 (8) (2021) 1973–1999.

[3] N. Sanaei, A. Fatemi, Defects in additive manufactured metals and their effect on fatigue performance: a state-of-the-art review, Prog. Mater. Sci. 117 (2021), 100724.

[4] H. Ghadimi, A.P. Jirandehi, S. Nemati, S. Guo, Small-sized specimen design with the provision for high-frequency bending-fatigue testing, Fatigue Fract. Eng. Mater. Struct. (2021).

[5] S. Lee, Z. Ahmadi, J.W. Pegues, M. Mahjouri-Samani, N. Shamsaei, Laser polishing for improving fatigue performance of additive manufactured Ti-6Al-4V parts, Opt. Laser Technol. 134 (2021), 106639.

[6] R. Molaei, A. Fatemi, N. Sanaei, J. Pegues, N. Shamsaei, S. Shao, P. Li, D. Warner, N. Phan, Fatigue of additive manufactured Ti-6Al-4V, Part II: The relationship between microstructure, material cyclic properties, and component performance, Int. J. Fatigue 132 (2020), 105363.

[7] M. Muhammad, P. Frye, J. Simsiriwong, S. Shao, N. Shamsaei, An investigation into the effects of cyclic strain rate on the high cycle and very high cycle fatigue behaviors of wrought and additively manufactured Inconel 718, Int. J. Fatigue 144 (2021), 106038.

[8] P. Nezhadfar, K. Anderson-Wedge, S. Daniewicz, N. Phan, S. Shao, N. Shamsaei, Improved high cycle fatigue performance of additively manufactured 17-4 PH stainless steel via in-process refining micro-/defect-structure, Addit. Manuf. 36 (2020), 101604.

[9] P. Nezhadfar, S. Thompson, A. Saharan, N. Phan, N. Shamsaei, Structural integrity of additively manufactured aluminum alloys: effects of build orientation on microstructure, porosity, and fatigue behavior, Addit. Manuf. (2021), 102292.

[10] A. Yadollahi, N. Shamsaei, Additive manufacturing of fatigue resistant materials: challenges and opportunities, Int. J. Fatigue 98 (2017) 14–31.

[11] S. Shao, M.M. Khonsari, S. Guo, W.J. Meng, N. Li, Overview: additive manufacturing enabled accelerated design of Ni-based alloys for improved fatigue life, Addit. Manuf. 29 (2019), 100779.

[12] A. Yadollahi, M. Mahtabi, A. Khalili, H. Doude, J. Newman Jr., Fatigue life prediction of additively manufactured material: effects of surface roughness, defect size, and shape, Fatigue Fract. Eng. Mater. Struct. 41 (7) (2018) 1602–1614.

[13] L. Sheridan, O.E. Scott-Emuakpor, T. George, J.E. Gockel, Relating porosity to fatigue failure in additively manufactured alloy 718, Mater. Sci. Eng.: A 727 (2018) 170–176.

[14] H. Bao, S. Wu, Z. Wu, G. Kang, X. Peng, P.J. Withers, A machine-learning fatigue life prediction approach of additively manufactured metals, Eng. Fract. Mech. 242 (2021), 107508.

[15] R.S. Haridas, S. Thapliyal, P. Agrawal, R.S. Mishra, Defect-based probabilistic fatigue life estimation model for an additively manufactured aluminum alloy, Mater. Sci. Eng.: A 798 (2020), 140082.

[16] P. Edwards, M. Ramulu, Fatigue performance evaluation of selective laser melted Ti–6Al–4V, Mater. Sci. Eng. A 598 (2014) 327–337.

[17] A. Yadollahi, M. Mahmoudi, A. Elwany, H. Doude, L. Bian, J.C. Newman Jr., Fatigue-life prediction of additively manufactured material: Effects of heat treatment and build orientation, Fatigue Fract. Eng. Mater. Struct. 43 (4) (2020) 831–844.

[18] A. Yadollahi, N. Shamsaei, S.M. Thompson, A. Elwany, L. Bian, Effects of building orientation and heat treatment on fatigue behavior of selective laser melted 17-4 PH stainless steel, Int. J. Fatigue 94 (2017) 218–235.

[19] G. Ziółkowski, E. Chlebus, P. Szymczyk, J. Kurzac, Application of X-ray CT method for discontinuity and porosity detection in 316L stainless steel parts produced with SLM technology, Arch. Civ. Mech. Eng. 14 (4) (2014) 608–614.

[20] G. Qian, Y. Li, D. Paolino, A. Tridello, F. Berto, Y. Hong, Very-high-cycle fatigue behavior of Ti-6Al-4V manufactured by selective laser melting: effect of build orientation, Int. J. Fatigue 136 (2020), 105628.

[21] A.R. Balachandramurthi, N.R. Jaladurgam, C. Kumara, T. Hansson, J. Moverare, J. Gårdstam, R. Pederson, On the microstructure of laser beam powder bed fusion alloy 718 and its influence on the low cycle fatigue behaviour, Materials 13 (22) (2020) 5198.

[22] T. Persenot, A. Burr, G. Martin, J.-Y. Buffiere, R. Dendievel, E. Maire, Effect of build orientation on the fatigue properties of as-built Electron Beam Melted Ti-6Al-4V alloy, Int. J. Fatigue 118 (2019) 65–76.

[23] R. Shrestha, J. Simsiriwong, N. Shamsaei, S.M. Thompson, L. Bian, Effect of build orientation on the fatigue behavior of stainless steel 316L manufactured via a laser-powder bed fusion process, 27th Annual Solid Freeform Fabrication Symposium Proceedings, 2016, pp. 605–616.

[24] A. Fatemi, R. Molaei, J. Simsiriwong, N. Sanaei, J. Pegues, B. Torries, N. Phan, N. Shamsaei, Fatigue behaviour of additive manufactured materials: an overview

of some recent experimental studies on Ti-6Al-4V considering various processing and loading direction effects, Fatigue Fract. Eng. Mater. Struct. 42 (5) (2019) 991–1009.

[25] M. Komarasamy, S. Shukla, S. Williams, K. Kandasamy, S. Kelly, R.S. Mishra, Microstructure, fatigue, and impact toughness properties of additively manufactured nickel alloy 718, Addit. Manuf. 28 (2019) 661–675.

[26] A.S. Johnson, S. Shao, N. Shamsaei, S.M. Thompson, L. Bian, Microstructure, fatigue behavior, and failure mechanisms of direct laser-deposited Inconel 718, Jom 69 (3) (2017) 597–603.

[27] Y.S.J. Yoo, T.A. Book, M.D. Sangid, J. Kacher, Identifying strain localization and dislocation processes in fatigued Inconel 718 manufactured from selective laser melting, Mater. Sci. Eng.: A 724 (2018) 444–451.

[28] R. Ghiaasiaan, M. Muhammad, P.R. Gradl, S. Shao, N. Shamsaei, Superior tensile properties of Hastelloy X enabled by additive manufacturing, Mater. Res. Lett. 9 (7) (2021) 308–314.

[29] S. Gribbin, J. Bicknell, L. Jorgensen, I. Tsukrov, M. Knezevic, Low cycle fatigue behavior of direct metal laser sintered Inconel alloy 718, Int. J. Fatigue 93 (2016) 156–167.

[30] V. Prithivirajan, M.D. Sangid, Examining metrics for fatigue life predictions of additively manufactured IN718 via crystal plasticity modeling including the role of simulation volume and microstructural constraints, Mater. Sci. Eng. A 783 (2020), 139312.

[31] B. Chen, J. Jiang, F.P. Dunne, Is stored energy density the primary meso-scale mechanistic driver for fatigue crack nucleation? Int. J. Plast. 101 (2018) 213–229.

[32] D. Wilson, W. Wan, F.P. Dunne, Microstructurally-sensitive fatigue crack growth in HCP, BCC and FCC polycrystals, J. Mech. Phys. Solids 126 (2019) 204–225.

[33] B. Hajshirmohammadi, M. Khonsari, Thermographic evaluation of metal crack propagation during cyclic loading, Theor. Appl. Fract. Mech. 105 (2020), 102385.

[34] B. Hajshirmohammadi, M. Khonsari, A simple approach for predicting fatigue crack propagation rate based on thermography, Theor. Appl. Fract. Mech. 107 (2020), 102534.

[35] C. Douellou, X. Balandraud, E. Duc, B. Verquin, F. Lefebvre, F. Sar, Rapid characterization of the fatigue limit of additive-manufactured maraging steels using infrared measurements, Addit. Manuf. 35 (2020), 101310.

[36] A.P. Jirandehi, M.M. Khonsari, On the determination of cyclic plastic strain energy with the provision for microplasticity, Int. J. Fatigue 142 (2021), 105966.

[37] A.P. Jirandehi, M. Khonsari, Microstructure-sensitive estimation of fatigue life using cyclic thermodynamic entropy as an index for metals, Theor. Appl. Fract. Mech. 112 (2021), 102854.

[38] V. Mortezavi, A. Haghshenas, M. Khonsari, B. Bollen, Fatigue analysis of metals using damping parameter, Int. J. Fatigue 91 (2016) 124–135.

[39] A. Haghshenas, M. Khonsari, Evaluation of fatigue performance of additively manufactured SS316 via internal damping, Manuf. Lett. 18 (2018) 12–15.

[40] R. Barnes, N. Hancock, E. Silk, The influence of vacancies upon the internal friction of polycrystalline copper, Philos. Mag.: A J. Theor. Exp. Appl. Phys. 3 (29) (1958) 519–526.

[41] K. Lücke, Ultrasonic attenuation caused by thermoelastic heat flow, J. Appl. Phys. 27 (12) (1956) 1433–1438.

[42] P. Southgate, Temperature dependence of internal friction in germanium, Phys. Rev. 110 (4) (1958) 855.

[43] V. Crupi, An unifying approach to assess the structural strength, Int. J. Fatigue 30 (7) (2008) 1150–1159.

[44] C. Zener, Internal friction in solids. I. Theory of internal friction in reeds, Phys. Rev. 52 (3) (1937) 230.

[45] F. Orban, Damping of materials and members in structures, Journal of Physics: Conference Series, IOP Publishing, 2011, p. 012022.

[46] J.D. Rogers, A method for determining material damping from driving point measurements, Iowa State University, 1986.

[47] A. Esin, W. Jones, A statistical approach to micro-plastic strain in metals, J. Strain Anal. 1 (5) (1966) 415–421.

[48] B. Chen, Understanding microstructurally-sensitive fatigue crack nucleation in superalloys, (2018).

[49] J. Chen, A.M. Korsunsky, Why is local stress statistics normal, and strain lognormal? Mater. Des. 198 (2021), 109319.

[50] G.I. Taylor, Analysis of plastic strain in a cubic crystal, Stephen Timoshenko 60th Anniversary Volume (1938) 218–224.

[51] B. JFw, R. Hill, A theoretical derivation of the plastic properties of a polycrystalline face-centred metal, Philos. Mag. 42 (1951) 1298–1307.

[52] J. Bishop, R. Hill, XLVI. A theory of the plastic distortion of a polycrystalline aggregate under combined stresses, Lond., Edinb., Dublin Philos. Mag. J. Sci. 42 (327) (1951) 414–427.

[53] G. Meneghetti, Analysis of the fatigue strength of a stainless steel based on the energy dissipation, Int. J. Fatigue 29 (1) (2007) 81–94.

[54] D. Rigon, V. Formilan, G. Meneghetti, Analysis of the energy dissipation in multiaxial fatigue tests of AISI 304L stainless steel bars, Procedia Struct. Integr. 13 (2018) 1638–1643.

[55] B. Hajshirmohammadi, M. Khonsari, On the entropy of fatigue crack propagation, Int. J. Fatigue 133 (2020), 105413.

[56] X. Wang, B. Chen, J. Sun, Y. Jiang, H. Zhang, P. Zhang, B. Fei, Y. Xu, Iron-induced oxidative stress stimulates osteoclast differentiation via NF-κB signaling pathway in mouse model, Metabolism 83 (2018) 167–176.

[57] C. Basaran, C.-Y. Yan, A thermodynamic framework for damage mechanics of solder joints, 1998.

[58] C. Basaran, S. Nie, An irreversible thermodynamics theory for damage mechanics of solids, Int. J. Damage Mech. 13 (3) (2004) 205–223.

[59] M. Amiri, M. Khonsari, Rapid determination of fatigue failure based on temperature evolution: fully reversed bending load, Int. J. Fatigue 32 (2) (2010) 382–389.

[60] J. Jang, M. Khonsari, On the evaluation of fracture fatigue entropy, Theor. Appl. Fract. Mech. 96 (2018) 351–361.

[61] G. Meneghetti, M. Ricotta, B. Atzori, A synthesis of the push-pull fatigue behaviour of plain and notched stainless steel specimens by using the specific heat loss, Fatigue Fract. Eng. Mater. Struct. 36 (12) (2013) 1306–1322.

[62] M. Naderi, M. Amiri, M. Khonsari, On the thermodynamic entropy of fatigue fracture, proceedings of the royal society a: mathematical, Phys. Eng. Sci. 466 (2114) (2010) 423–438.

[63] O. Andreau, I. Koutiri, P. Peyre, J.-D. Penot, N. Saintier, E. Pessard, T. De Terris, C. Dupuy, T. Baudin, Texture control of 316L parts by modulation of the melt pool morphology in selective laser melting, J. Mater. Process. Technol. 264 (2019) 21–31.

[64] A.M. Handbook, Vol. 11, 9: th edition, American Society of, p. 200.